Generalized Data-Driven Model to Minimize Current Ringing in DAB Power Converter

Lopez Gajardo, Miguel; Gómez, Pere Izquierdo; Mijatovic, Nenad; Pérez, José Rodríguez ; Dragicevic, Tomislav

Published in:
IEEE Journal of Emerging and Selected Topics in Industrial Electronics

Link to article, DOI:
10.1109/JESTIE.2023.3324519

Publication date:
2024

Document Version
Peer reviewed version

Generalized Data-Driven Model to Minimize Current Ringing in DAB Power Converter

Miguel López Gajardo, *Student Member, IEEE*, Pere Izquierdo Gómez, *Student Member, IEEE*, Nenad Mijatovic, *Senior Member, IEEE*, José Rodríguez Pérez, *Life Fellow, IEEE*, and Tomislav Dragičević, *Senior Member, IEEE*

***Abstract*—The present paper identifies the root causes of current ringing in a Dual Active Bridge (DAB) power converter and proposes a novel methodology to design the magnetic tank (transformer, primary and secondary inductances) configuration to minimize it. In particular, two metrics proportional to the current harmonic content on each transformer side are correspondingly proposed based on a steady-state frequency analysis of primary and secondary ac voltages and impedance of the magnetic tank. To get the metrics, different combinations of dv/dt, switching frequency, primary and secondary inductance configuration, and stray capacitance of the magnetic tank (model inputs) are simulated to generate primary and secondary harmonic current indicators (model outputs). Then, a machine-learning model is trained to predict the harmonic current metrics for each given operating setpoint. The model is able to make predictions beyond its training data, therefore generalizing to unseen inputs and enabling rapid evaluation of various designs. Experimental results are presented to evaluate the performance of the metric model for 4 different magnetic tank configurations. Designers can use the methodology to rapidly analyze the generation of current ringing under multiple operating parameters, identifying operating zones with low harmonic content and reduced sensitivity to parameter shifts for the converter's operation.**

***Index Terms*—Dual Active Bridge, frequency-domain analysis, machine learning, magnetics, current ringing.**

I. Introduction

THE Dual Active Bridge (DAB) [1]–[4] is a dc/dc power converter that has a number of desirable features such as input/output galvanic isolation, bidirectional power flow, and wide voltage conversion gain range. This allows the use of high-frequency magnetics, which provide high power density, and reduce the volume and weight of the converter. All these characteristics make the converter suitable for a number of applications, including on-board battery chargers, e-mobility, and multi-port systems, to name a few.

Ringing is a phenomenon previously reported in the literature, observed in electronic circuits as a high-frequency voltage and current oscillation [5], [6]. Due to stray components present in the circuit (parasitics in components, circuit layout, line routing), the high-frequency behavior of the circuit will generate undesired impedance. For instance, when high dv/dt is generated, high-frequency voltage harmonic content is produced, and at high frequency the stray capacitances provide a low impedance path to these harmonics, generating current ringing. Similarly, when high di/dt is produced, high-frequency current harmonic content is generated, and the stray inductances at high frequency behave as unexpected high impedance, causing voltage ringing. Nowadays, the use of wide bandgap semiconductors, such as SiC and GaN, has led to the possibility of high switching frequency (hundreds of kHz to few MHz [7]) in power converters including DABs. This can lead to high dv/dt, high-frequency harmonic content, which makes ringing more likely to happen. Ringing can generate increased losses, Electromagnetic Interference (EMI), and overvoltages that can even damage the electronic devices [8]–[11]. Thus, the ringing phenomenon must be studied, aiming to develop techniques to guarantee electromagnetic compatibility in the target application and improve the high-frequency performance of the power electronic converter.

In the literature, different methods have been proposed to deal with the ringing in power electronic converters. Two main groups of approaches can be identified. A first approach is to reduce the dv/dt using snubber devices, i.e. [12], [13]. [9] proposed a methodology to determine a relation between the voltage spikes, dv/dt and stray capacitance (winding capacitance) of the transformer, which can help in sizing the snubber capacitor to reduce the voltage spike in the transformer side. The main disadvantages are that it will increase the difficulty to achieve soft-switching when the output capacitance is increased, and that higher turn-on switching losses at hard-switching are expected, since more energy is stored in the drain-source capacitance of the power semiconductors [2], [14], [15]. Despite these negative effects, snubber circuits can increase the efficiency of the converter under certain operating points by reducing ringing [16]–[18]. In a similar manner, another way is to select or reduce the dv/dt via active methods. In this way, dv/dt can be limited by an active gate control, which can adjust how fast the semiconductor switching is achieved [19]–[22]. When large parasitic parameters are present in the circuit, the reduction of the dv/dt or di/dt by the active gate driver might not be enough to reduce the ringing. For instance, when dealing with long PCB traces, or disposing of a transformer or inductance with too high stray parameters. In these scenarios, a ringing reduction can consider how different configurations for the inductance array within the magnetic tank can affect the ringing, for different dv/dt or switching frequencies, increasing the complexity of the analysis. A second approach is to refine the impedance model of the power converter components on a wide frequency domain. In this direction, the literature focuses on analyzing the stray components to reduce their size and/or consider measures to deal with them in the design stage of the converter.

Particularly, stray capacitance in magnetic components reduces their impedance at high frequency [23]. In order to reduce parasitic capacitance in transformers, improvements in the winding layout of planar transformers [24] and core shielding [25] have been reported to reduce common mode (CM) noise and thus current ringing. Additionally, a discussion on the trade-offs to reduce stray capacitances in the design stage of a planar transformer was reported in [26]. One of the difficulties of this approach is that the design effort to reduce stray capacitance and time consumption to analyze how the current ringing is produced under different scenarios might be significantly high. Thus, while both approaches can be used to reduce ringing, a methodology that can more directly estimate the current ringing mechanism is highly desirable to complement them and make the design process faster and more accurate. Such a model may consider features related to component parameters and voltage waveforms, including component tolerance, thermal drift, or aging of the magnetics.

This article overcomes the identified limitation. First, it describes theoretically the relationship between the harmonic content of the voltage and the impedance of the magnetic tank, which generates current ringing on the transformer's primary and secondary sides, based on the model described in [27]. Then, a metric is proposed, which measures how the current ringing harmonics on each side behave based on different magnetic tank configurations and voltage waveform features. This metric can be used to visualize how different primary and secondary inductances, stray capacitances of the inductors, dv/dt, and switching frequencies affect the current ringing performance. A machine-learning model is trained to represent a generalized model of the harmonic content of the magnetic tank currents, allowing rapid assessment of different converter operations and magnetic tank designs. This can help to identify operating points with low current ringing and decreased sensitivity to parameter shifts for optimal converter operation. The model is shown to be able to learn the main features contained in its training data set. Experimental results validate the theoretical insights into the harmonic behavior of the current ringing of four magnetic tank designs.

The paper is organized as follows. Section II describes the DAB power converter, its principle of operation, and briefly illustrates its modulation aspects. Section III explains theoretically the relationship between the voltage waveform and the impedance of the magnetic tank to elucidate the root causes of the current ringing phenomenon. Section IV develops the methodology to create a machine-learning (ML) model of the harmonic current content based on a set of parameters that define the voltage and impedance features. The model is then used to quickly and precisely evaluate the current ringing for different magnetic tank configurations. Section V shows experimental results of current ringing for 4 different magnetic tank configurations and switching frequencies, thereby validating the model obtained in Section IV. Section VI elaborates a discussion on the use of a metric and ML (ANN) to study the harmonic current content and thus the current ringing in the DAB converter. Finally, Section VII concludes the paper by summarizing the main results and discussing potential future work directions.

II. Topology and Principle of Operation

The topology of the DAB power converter is illustrated in Fig. 1.a. It is configured as two full bridges connected between themselves via a magnetic tank, which comprises a transformer, and an array of inductances that can be simplified to an equivalent inductance L on the primary side (high voltage side, considering $n > 1$). The simplified model of the converter is illustrated in Fig. 1.b, where two voltage sources feed the inductance L in order to transfer power from one side to the other, while the transformer provides galvanic isolation and adjusts the voltage from the secondary side. The operation of the converter considers two stages, the controller and the modulation [2]–[4]. In the first one, a control algorithm determines how the converter should act to follow the reference (which might be output voltage, current, or both), and this is received by the modulator, which generates corresponding switching signals for the MOSFETs.

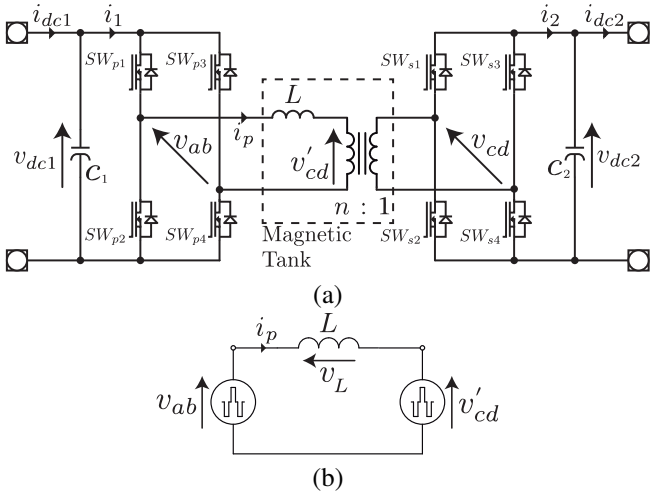

Fig. 1. The DAB power converter. (a) Topology for primary and secondary full-bridges as active bridges; (b) Simplified model.

There are different modulation schemes studied in the literature to set the voltage waveform of the primary and secondary sides to transfer power accordingly. A broad classification identified in the literature is based on the number of control angles managed. Single Phase Shift (SPS) modulation manipulates the phase shift D_3 between the primary and secondary ac voltages generated by the corresponding full-bridges (where $D_1 = D_2 = 1$, meaning that each full-bridge works as a two-level voltage source that provides $\pm v_{dc}$ at 50% duty cycle). In Dual Phase Shift (DPS) modulation, two variables are handled, i.e. the phase shift D_3 and D_1 or D_2, where a proportion between the two is defined ($D_1 = \alpha D_2$). Finally, in Triple Phase Shift (TPS), a zero voltage is applied on each full-bridge and the phase shift is determined by controlling D_1, D_2 and D_3, as illustrated in Fig. 2.

III. Current ringing in the magnetic tank

High dv/dt and high order switching frequency harmonics of the primary and secondary voltage waveform can generate significant high-frequency content in the current of the magnetic tank [27]. The inductances and the transformer comprising

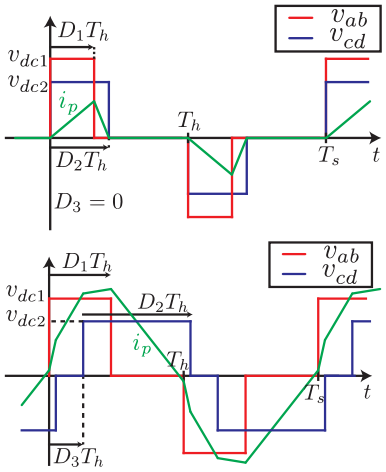

Fig. 2. Waveform for TPS modulation [4]. Top: Triangular mode; Bottom: Trapezoidal mode.

the magnetic tank at high frequency do not behave purely as RL impedance, because the stray capacitance components represent a low impedance path for high-frequency voltage content. This generates a high-frequency current ringing in either the primary or secondary side, which results in oscillating energy that generates losses [8] and EMI [10], [11]. Both of these effects are undesirable. To analyze this, both voltage and impedance models should be considered.

Snubber circuits [9], [12], [13] are used to limit the dv/dt and reduce the overvoltage during switching [9], which would otherwise provide high-frequency harmonics to the magnetic tank.

There are two possible approaches that can be considered to analyze the current ringing: steady-state and time-frequency analysis. The frequency behavior of the voltage waveform depends on the switching frequency, the duty cycle, and its rising and falling edges. Thus, the frequency content of the voltage signal is significant during dv/dt, where its corresponding energy is stored in the magnetic tank. Afterwards, this amount of stored energy decreases as a damped current oscillation, and the process is repeated as new dv/dt occur, depending on the modulation implemented. In this sense, a time-frequency approach analyzes how the current harmonics are behaving in time. Alternatively, the time-series data of the voltage waveform can be used to estimate its frequency behavior. The latter approach can be considered as a steady-state frequency analysis of the voltage signal. To illustrate this notion, one may consider a 50% duty cycle voltage waveform at 50kHz switching frequency (f_{sw}), for two different rising and falling times (t_r), as in Fig. 3.a. For example, t_r represents the time required for the voltage to switch from one state to the other, which is inversely proportional to the dv/dt of the commutation. Thus, both the voltage slope and switching frequency contribute significantly to the high-frequency content, as is depicted in Fig. 3.b (for different t_r) and 3.c (for different f_{sw}). From Fig. 3.c, we observe that higher switching frequencies increase the magnitude and distance of the frequencies between each other, generating different high-frequency harmonic content. Besides, m/t_r (with m positive

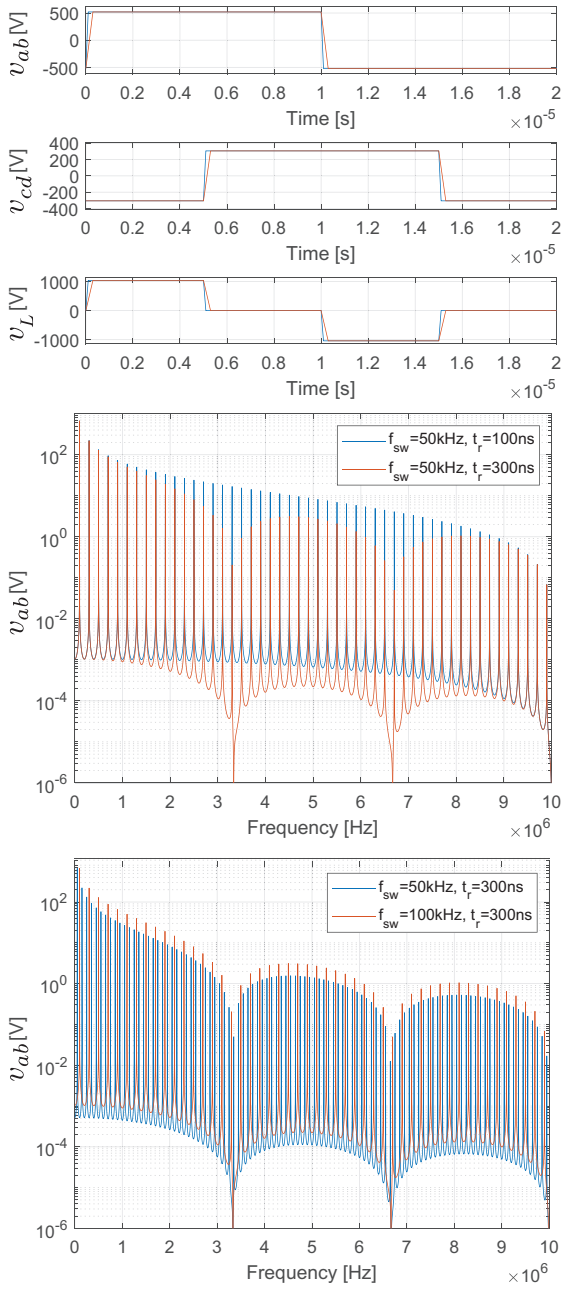

Fig. 3. Time and frequency behavior of voltage ac waveform under different dv/dt (or rising/falling time) and switching frequency, for $v_{dc1} = 520V$, $v_{dc2} = 306V$, $n = 1.7$, $D_1 = D_2 = 1$ and $D_3 = 0.5$. (a) v_{ab}, v_{cd} and v_L behavior over time for $t_r = 100ns$ and $300ns$ (blue and red signal, respectively); v_{ab} over frequency domain for different dv/dt (b) and f_{sw} (c).

integer) are the frequencies where a minimum voltage magnitude are located. Summarizing, the first approach provides information about the frequency content in time, while the second approach estimates the average frequency content in the time-series data. Theoretical analysis and experimental results presented in the sequel will provide further clarification on these subjects.

A. Impedance model of the Magnetic Tank

Based on Fig. 1.a, the inductance of the DAB can be located in the primary side (L_p), in the secondary side (L_s), or in both

sides, while maintaining in any case the modeled equivalent value of L for power transfer based on Eqn. (1). Thus, it can be configured as an array of a series of inductances on each side to reach the desired value of L. Besides, the stray components of the inductances and transformer are also relevant to consider at high frequencies. Core and wire resistance (R_{fe} and R_{cu}), stray capacitance on primary (C_p), secondary (C_s), and primary-core-secondary (C_{ps}) are considered. Fig. 4 depicts the magnetic tank with the stray parameters.

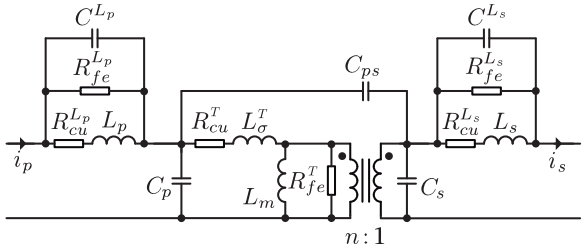

Fig. 4. Magnetic tank of DAB power converter considering stray parameter for primary and secondary side inductances L_p and L_s, respectively.

$$L = L_p + n^2 \cdot L_s \tag{1}$$

In order to have a model for the input impedance at the high (primary) and low (secondary) side of the magnetic tank, a Thevenin equivalent model can be obtained based on the stray parameters of the inductor and transformer [27] considering inductances in primary and secondary sides. The equations for the primary (input) and secondary (output) impedance are defined in (2).

$$\begin{aligned}
Z_{in}^{p} &= R_{cu}^{T} + L_\sigma^{T}(jw) \\
&+ \underbrace{\frac{L_p \cdot R_{fe}^{L_p}(jw) + R_{cu}^{L_p} \cdot R_{fe}^{L_p}}{jw(L_p + C^{L_p} R_{cu}^{L_p} R_{fe}^{L_p}) + R_{cu}^{L_p} + R_{fe}^{L_p} - w^2 C^{L_p} L_p R_{fe}^{L_p}}}_{\text{Primary side parameters}} \\
&+ \underbrace{\frac{n^2 \cdot R_a(L_s(jw) + R_{cu}^{L_s})}{R_a + n^2(R_{cu}^{L_s} + L_s(jw)) + C_a n^2 R_a(jw)(R_{cu}^{L_s} + L_s(jw))}}_{\text{Inductor's secondary side \& transformer parameters}} \\
&\text{where } R_a = \frac{n^2 R_{fe}^{T} R_{fe}^{L_s}}{R_{fe}^{T} + n^2 R_{fe}^{L_s}}, \\
&C_a = C_p + \frac{C^{L_s} + C_s}{n^2} + (1 - 1/n)^2 \cdot C_{ps}/4 \\
Z_{in}^{s} &= \frac{R_{cu}^{T} + L_\sigma^{T}(jw)}{n^2} \\
&+ \underbrace{\frac{R_{fe}^{L_s}(L_s(jw) + R_{cu}^{L_s})}{jw(L_s + C^{L_s} R_{cu}^{L_s} R_{fe}^{L_s}) + R_{cu}^{L_s} + R_{fe}^{L_s} - w^2 C^{L_s} L_s R_{fe}^{L_s}}}_{\text{Secondary side parameters}} \\
&+ \underbrace{\frac{R_b(L_p(jw) + R_{cu}^{L_p})}{n^2 R_b + (R_{cu}^{L_p} + L_p(jw))(1 + C_b R_b(jw))}}_{\text{Inductor's primary side \& transformer parameters}} \\
&\text{where } R_b = \frac{R_{fe}^{T} R_{fe}^{L_p}}{n^2(R_{fe}^{T} + R_{fe}^{L_p})}, \\
&C_b = n^2(C^{L_p} + C_p) + C_s + (n-1)^2 C_{ps}/4
\end{aligned} \tag{2}$$

IV. Methodology to Select Magnetic Tank Configurations

The origin of the current ringing is a function of the impedance and the voltage, where there is a certain range of frequencies based on the magnetic tank parameters where the impedance is low and so the voltage generates a high current oscillation. Based on Eqn. (2), this effect is caused by the stray parameters of the transformer and the inductance at the secondary and primary side, respectively. These stray parameters can be reduced up to a certain point in the design stage, and once defined, certain configurations of these parameters are expected to reduce the harmonic content in both the primary and secondary sides for the applied primary and secondary voltages. In this sense, depending on the frequency content of both primary and secondary voltage sources and the impedance seen from the primary and secondary sides of the magnetic tank, it is possible to evaluate the current performance for different combinations of parameters in the magnetic tank.

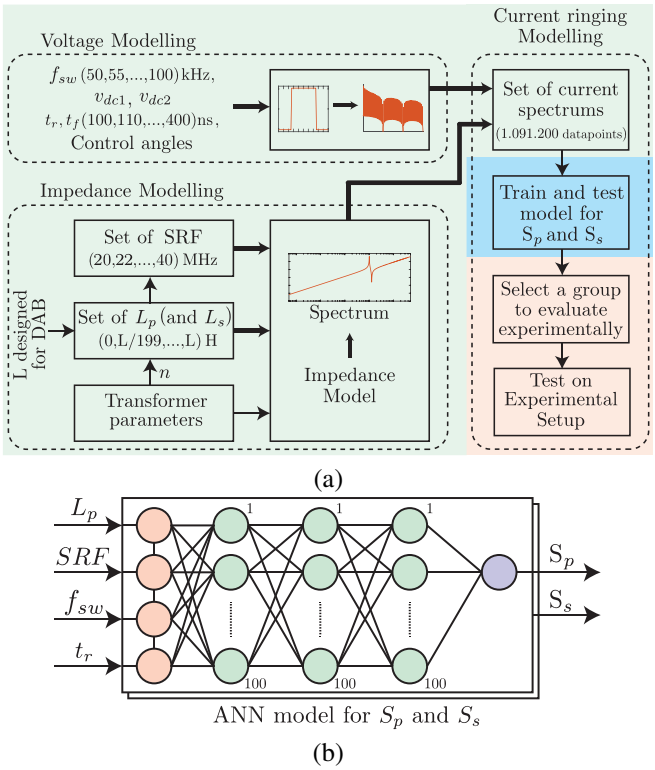

Fig. 5. Methodology and ML model proposed to evaluate current ringing. (a) Methodology (MATLAB, Python, and experimental work over the green, light blue and red background); (b) ANN models for the metrics S_p and S_s.

This article proposes a novel machine learning methodology to model the harmonic current behavior in the magnetic tank, in order to evaluate which design configuration achieves low harmonic content at a certain switching frequency, input and output dc voltages, and dv/dt, considering tolerance and uncertainty in the component values. The proposed procedure is explained in Fig. 5.a. MATLAB simulation was used to synthetically generate the data set, while Python was used to train and test the machine learning model. The steps are enumerated as follows and are described in more detail in the following paragraphs:

1) Generate voltage spectrum data set.
2) Generate impedance spectrum data set.
3) From 1 and 2, obtain current spectrum data set.

TABLE I
PARAMETERS OF TWO INDUCTANCES TO USE IN THE MAGNETIC TANK.

	Inductance 1	Inductance 2
Part number	PQ2617BHA-3R3K	PQ2617BHA-4R7K
$L[\mu H]$	3.49	4.7
$R_{cu}[m\Omega]$	2.5	2.5
$R_{fe}[k\Omega]$	2.44	2.44
$SRF[MHz]$	40	30
$C[pF]$	4.79	5.98

4) Calculate a parameter proportional to the current harmonic content, defined as metrics S_p and S_s for primary and secondary sides.
5) Train and test a machine learning model of the metrics S_p and S_s based on voltage and impedance parameters defined in 1 and 2.
6) Use the model to quickly find an optimal combination of L_p and L_s and test these combinations experimentally.

To get the voltage spectrum data set, we define a set of possible voltages that can be applied at fixed input and output dc voltage, and fix the control angles to achieve maximum output power [28] ($D_1 = D_2 = 1$, $D_3 = 1/2$, $v_{dc1} = 520V$, $v_{dc2} = 306V$). A set of 11 switching frequency ($f_{sw} = [50, 55, ..., 100]$kHz) and 31 rising time ($t_r = [100, 110, ..., 400]$ns) were considered to generate 11x31=341 possible voltages for each primary (v_{ab}) and secondary side (v_{cd}), based on the nominal values of v_{dc1} and v_{dc2}, respectively. For simplicity, falling and rising times are considered equal. Thus, different values of dv/dt are evaluated based on t_r, and the dc voltage of the corresponding side. To determine the range of t_r to test, the converter was tested previously in the laboratory under different power operations for the same input and output dc voltage. Thus, t_r changes in the range [100,400]ns approximately, depending on the current during the switching instants [29]. Then, through FFT, the harmonic content of the voltage waveform can be produced and assessed for each of the 11x31 cases, for both the primary and secondary voltage spectrum.

To get the impedance spectrum data set, different configurations for the primary and secondary impedances in the magnetic tank can be simulated. In order to do this, the parameters of the transformer and the inductance of the primary and secondary sides are used as alternatives to construct the magnetic tank, based on Eqn. (2). Then, based on the power transfer inductance L and the turns ratio of the transformer, we generate a vector of 200 possible L_p and L_s, based on Eqn. (1). Besides, the manufacturer facilitates the typical self-resonance frequency of the inductance in order to calculate the stray capacitance based on Eqn. (3), which can be used to calculate different configurations of inductances in series. We considered 16 values for the self-resonance frequency SRF ($SRF = [20, 22, ..., 50]$MHz), based on the typical values for this parameter specified in the inductor datasheet. For the same purpose, the series equivalent for the core and copper resistances can be calculated based on Eqn. (4). This generates a set of 200x16 possible configurations of the magnetic tank.

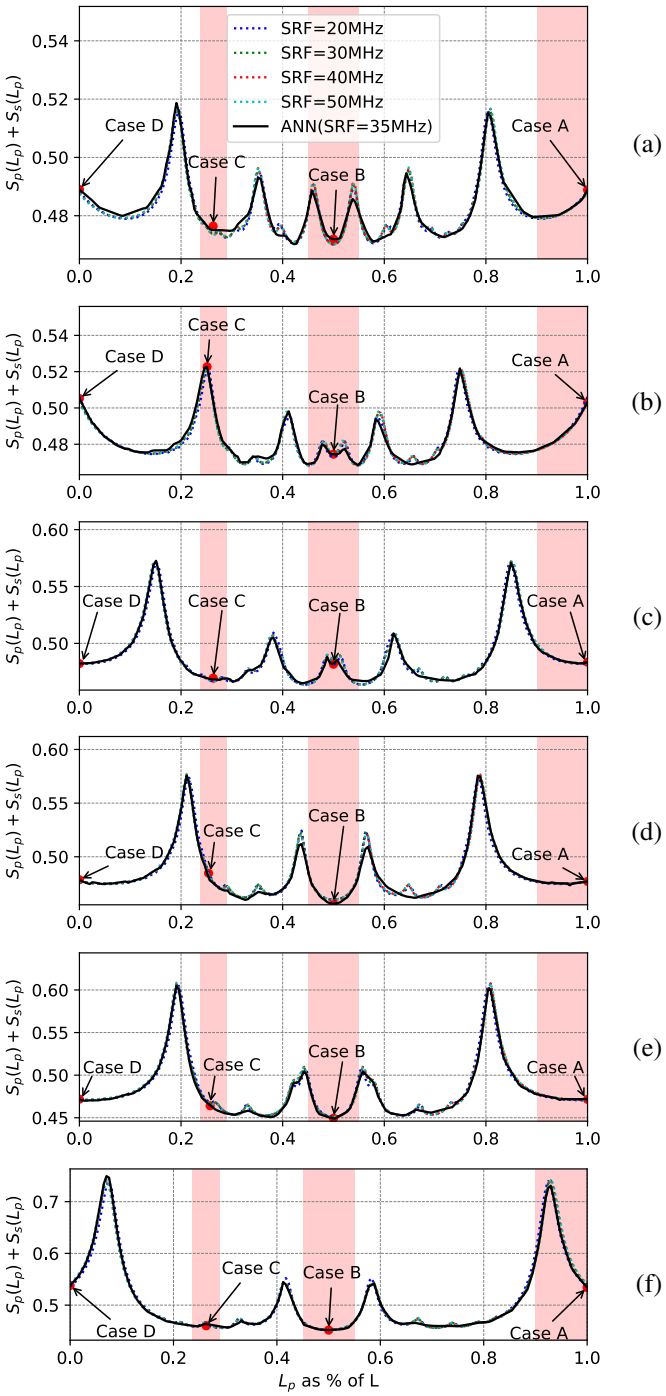

Fig. 6. ANN model of $S_p + S_s$ for different f_{sw}, at $t_r = t_f = 150$ns. Light red background zones represent $\pm 10\%$ inductance tolerance facilitated by the manufacturer. (a) $f_{sw} = 50$kHz; (b) $f_{sw} = 60$kHz; (c) $f_{sw} = 70$kHz; (d) $f_{sw} = 80$kHz; (e) $f_{sw} = 90$kHz; (f) $f_{sw} = 100$kHz.

$$SRF = \frac{1}{2\pi\sqrt{L_{eq} \cdot C_{eq}}} \rightarrow C_{eq} = \frac{1}{(2\pi \cdot SRF)^2 L_{eq}} \quad (3)$$

$$C_{eq} = C/n_{series} \quad L_{eq} = n_{series} \cdot L_b \quad R_{eq} = n_{series} \cdot R \quad (4)$$

To generate the current spectrum data set based on the voltage and impedance configurations, we obtain the harmonic

TABLE II
TRANSFORMER PARAMETERS OF THE MAGNETIC TANK.

	Value
Turn ratio (n)	1.7
$L_m[\mu H]$	8100
$L_\sigma^T = L_\sigma^{T_p} + n^2 L_\sigma^{T_s}[\mu H]$	132
$R_{cu}^T = R_{cu}^{T_p} + n^2 R_{cu}^{T_s}[m\Omega]$	37.2
$R_{fe}^T[k\Omega]$	197
$C_p + C_s/n^2[pF]$	224
$C_{ps}[nF]$	2.35

content of 11x31x16x200=1.091.200 primary and secondary currents (i_{pp} and i_{ss}). It is worth noting that previous frequency analysis of the magnetic tank impedances and voltage waveforms has to be done to select the values to generate the data set, in order to represent the current harmonic content.

In order to analyze the performance of different configurations, the use of an indicator is proposed. The L1 norm of the spectrum (the sum of the harmonics) can be considered, which can evaluate how spread out the harmonic content is. The L2 norm (the square root of the sum of the square of the harmonics) can also be used as a measure of efficiency, because power loss is a function of the square of the harmonics and the ac resistance of the inductance. In both cases, low values represent low harmonic content. Both values may change proportionally with the amplitude, which complicates the comparisons between different voltage and magnetic tank impedances. For a sinusoidal waveform, the Total Harmonic Distortion (THD) is a good choice because it quantifies how much harmonic content is present in the signal with respect to its fundamental harmonic. It is expected that the magnitudes of the high-frequency content are small, and squaring each harmonic can decrease the influence of the ringing content on the overall metric for different designs. To mitigate this, the indicator used to study the current ringing is shown in Eqn. (5), where $x = pp$ refers to primary (S_{pp}) and $x = ss$ for secondary (S_{ss}) harmonic current metrics. We consider a maximum harmonic frequency of $f_{max} = 20$MHz.

$$S_x = \frac{\left(\sum_{j=1}^{f_{max}/f_{step}} i_x(f_{step} \cdot j)\right) - i_x(f_{sw})}{i_x(f_{sw})} \tag{5}$$

To generate a model that can represent the harmonic content of i_p and i_s in the metrics S_p and S_s, two steps were considered. First, identify relevant inputs of the model, and second, train and validate the model. The harmonic content of the current depends on the inductance value on the primary side, the rising and falling times (considered equal to t_r), the switching frequency f_{sw}, and the stray capacitances on the primary and secondary side inductances (determined by SRF from Eqn. (3)). Based on Eqn. (1), L_s is dependent on L_p and L, so only considering L_p or L_s as an input of the model is sufficient. On the inductance datasheet, in order to quantify the stray capacitance, the typical SRF value is given. More than that, there is no information about how it can change due to temperature, aging or other factors. It is expected that the stray capacitance of the inductance and the transformer

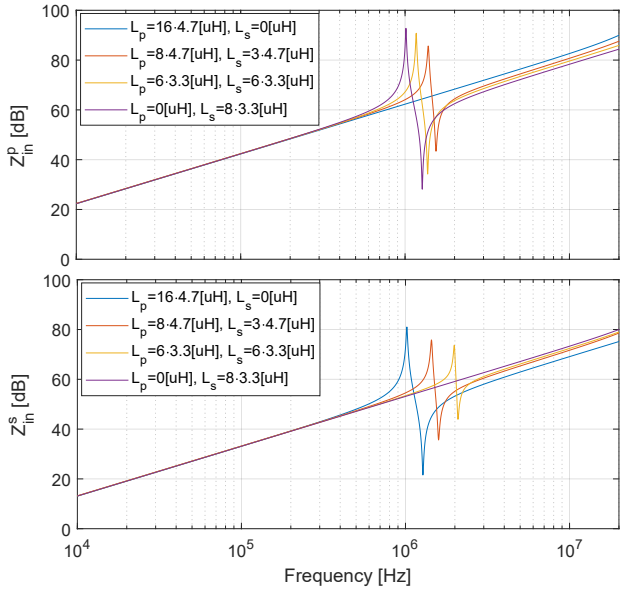

Fig. 7. Impedance of the magnetic tank under different configurations. Top: Impedance on the primary side Z_{in}^p; Bottom: Impedance on the secondary side Z_{in}^s.

will have an important effect on how the ringing current will behave [27]. The Artificial Neural Network (ANN) structure is shown in Fig. 5.b. Thus, an ANN model is used to estimate the metrics S_p and S_s, originated from the inputs L_p, f_{sw}, t_r and SRF. The data (inputs and outputs of the model) are normalized between 0 and 1. The *pytorch* and *scikit-learn* *k-fold* packages were used for training and validation of 5 k-fold cross-validation (i.e. 5 groups of data where 80% is training data and 20% is testing data). The ANN has, for each metric, 3 hidden layers (HLs) of 100 units each, *ReLU* as the activation function on each HL, the *Adam* optimizer, and the *SmoothL1loss* function, trained in 200 epochs and resulting in an average loss for each k-fold result equal to 2.84e-6 and 3.4e-6 for S_p and S_s models, respectively.

To compare the effect of primary and secondary harmonic content in the high-frequency current, the sum of S_p and S_s is proposed. The consideration to use this is explained in Appendix VIII-A. The resulting $S_p + S_s$ for 6 switching frequencies are illustrated in Fig. 6 to evaluate the performance of the metrics for the ANN model. The dv/dt was fixed to $t_r = t_f = 150ns$ for the primary and secondary sides. The results show that different minimum and maximum joint current harmonic content ($S_p + S_s$) are represented by the curves, which depend on different inductance values, stray capacitances, switching frequencies and dv/dt (represented by L, SRF, f_{sw} and t_r, respectively). The design point should lie away from the maximum peaks.

There are potentially a big number of possible parameters to consider that can affect the current harmonic content in the magnetic tank, for both voltage and impedance parameters of the components modeled. Besides, the bandwidth to consider in the analysis can be potentially high, particularly in high-frequency power supplies that use SiC or GaN semiconductor technology. By using an ML model, multiple design scenarios

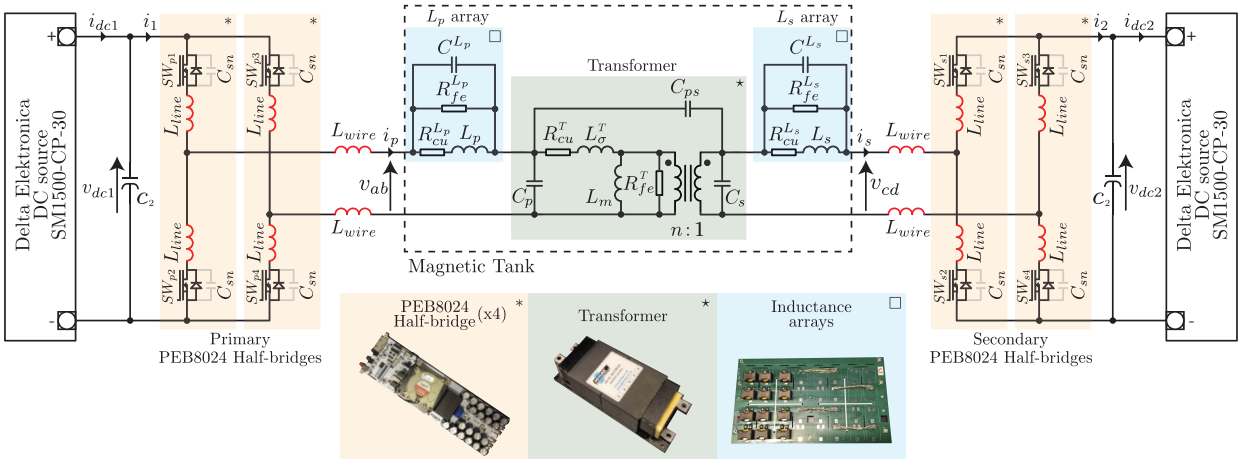

Fig. 8. DAB configuration considering the main stray components in the circuit.

can be rapidly generated to study in the design stage how the current harmonic content will behave for different sets of inputs. It can be considered that the switching frequency will remain practically constant throughout the converter's entire lifespan. However, the inductance values (L_p and L_s) and stray capacitance can potentially vary due to tolerance or parameter shifts. Due to the large number of possible combinations of parameters, the ML model can be employed to analyze the harmonic current behavior in a more efficient manner than with an analytical model.

To evaluate the methodology proposed, 4 different magnetic tank configurations were considered in the experimental validation (named cases A to D). The selection was based on the inductances defined in Table I and their combinations that result in a similar total inductance when accounting for the turns ratio of the transformer, based on Eqn. (1). They range from inductance only in the primary side ($[L_p, L_s] = [L, 0]$, case A) to only in the secondary side ($[L_p, L_s] = [0, L/n^2]$, case D). These cases were illustrated in Fig. 6. Note that the light red background zones on each case represent 10% tolerance for each case, which is facilitated by the manufacturer.

Based on Eqn. (2) and the parameters specified in Table I and II, the Bode diagram of 4 magnetic tank configuration cases (A to D) are illustrated in Fig. 7. The resonance frequency moves to a higher frequency on the side with a higher inductance, but the contrary effect is generated on the opposite side (primary or secondary). Based on this, it is expected that for certain primary and secondary voltage waveforms there exists a combination of inductances where the harmonic content of the current ringing is balanced between the primary and secondary sides for the selected metric.

V. Experimental Results

The experimental setup considers 4 Imperix PEB8024 half-bridges configured as shown in Fig. 8, which include SiC MOSFETs (C2M0080120D). Each MOSFET includes a snubber capacitor C_{sn} of $1nF$ and $3nF$ on the primary and secondary half-bridges, respectively, in order to limit their dv/dt. Deadtime is set to 600ns. A Bbox RCP system platform was used to implement SPS modulation and test different switching frequencies at different phase-shifts, to achieve similar i_p, i_s, and output power. We used the instruments LPA05 Impedance Analyzer, PSM1735, and N4L Impedance Analysis Interface to estimate the parameters of a transformer (based on [30]) and two inductances of 3.3 μH and 4.7 μH (see Tables I and II). The instruments cannot measure capacitance values smaller than 100 pF and resistances lower than 1 $m\Omega$, so for the inductors, we used the datasheet values for the copper losses, and the self-resonance frequency and inductor value to estimate the stray capacitance.

Thus, four magnetic tank designs were tested for 50 and 100kHz. The results from the oscilloscope data at f_{sw}=100kHz are shown in Fig. 9. The current ringing depends on the transformer side where the dv/dt occurs. During high dv/dt periods, more voltage harmonic content is produced. Besides, the bigger the current ringing, the lower the inductance on the corresponding side. When the inductance is only in the primary (or secondary) side (cases A and D, respectively), the current on the corresponding side is filtered. This occurs because the resonance frequency of the magnetic tank on the corresponding side increases significantly. When there are inductances on both sides (cases B and C), a current ringing appears on each side for the tested parameters. The spectrum of i_p and i_s are included in the last two rows of Fig. 9. Note that the spectrum is more spread on the side where lower inductance is used.

With respect to the voltage waveform, from Fig. 9 it can be inferred that there is a bigger voltage oscillation in the secondary side (v_{cd}) than the primary side (v_{ab}), where the current magnitude is greater. For the secondary side voltage v_{cd} (second row of Fig. 9), larger oscillations are appreciated where the magnetic tank does not consider inductances in the secondary side (Fig. 9.a) and higher current ringing is visualized. The reason might be the following. From Fig. 8, the current i_p and i_s is passing through L_{wire} on each side, which represent an equivalent line inductance for the wired connection between half-bridges bus bars and the magnetic tank. It is expected that on these inductances will be generated a voltage as a function of the current and the inductance size, which will be seen in v_{ab} and v_{cd} changing the voltage

TABLE III
EXPERIMENTAL RESULTS OF 4 INDUCTANCE CONFIGURATION FOR THE INDICATORS S_p, S_s AND $\Sigma = S_p + S_s$, UNDER DIFFERENT SWITCHING FREQUENCIES $f_{sw} = [50 : 10 : 100]kHz$, ADJUSTING $D_3 = [0.15 : 0.025 : 0.275]$ RESPECTIVELY. (A) $L_p = 16 \cdot 4.7\mu H$, $L_s = 0\mu H$; (B) $L_p = 8 \cdot 4.7\mu H$, $L_s = 3 \cdot 4.7\mu H$; (C) $L_p = 6 \cdot 3.3\mu H$, $L_s = 6 \cdot 3.3\mu H$; (D) $L_p = 0\mu H$, $L_s = 8 \cdot 3.3\mu H$.

	$f_{sw} = 50kHz$			$f_{sw} = 60kHz$			$f_{sw} = 70kHz$			$f_{sw} = 80kHz$			$f_{sw} = 90kHz$			$f_{sw} = 100kHz$		
Case	S_p	S_s	Σ	S_p	S_s	Σ	S_p	S_s	Σ	S_p	S_s	Σ	S_p	S_s	Σ	S_p	S_s	Σ
(A)	0.80	0.99	1.80	0.79	0.97	1.771	0.71	0.91	1.621	0.63	0.84	1.486	0.57	0.77	1.352	0.52	0.75	1.279
(B)	0.89	0.86	1.758	0.79	0.77	1.571	0.80	0.77	1.580	0.72	0.71	1.441	0.66	0.65	1.316	0.61	0.60	1.219
(C)	0.94	0.85	1.802	0.93	0.84	1.778	0.84	0.75	1.604	0.77	0.68	1.462	0.71	0.63	1.341	0.66	0.57	1.238
(D)	1.00	0.81	1.823	0.99	0.80	1.801	0.95	0.73	1.691	0.88	0.65	1.540	0.75	0.59	1.349	0.77	0.53	1.315

generated by the primary and secondary full-bridges. Fig. 10 shows a comparison between theoretical and experimental v_{cd} spectrum for two magnetic tank designs, with inductance only in primary and secondary side (Fig. 10.a and 10.b, respectively). Thus, theoretical and experimental voltage spectrum are different in the high frequency side, particularly where higher current ringing is appreciated. This will generate higher current harmonics and increasing the metrics on this side.

Table III summarizes the results obtained by calculating the metrics S_p and S_s based on Eqn. (5) using the measured currents i_p and i_s from the oscilloscope data, which works as an indicator for the different tested f_{sw}. Due to a small mismatch of the equivalent inductance value L in each case, the time-series primary and secondary currents of each designed inductance were normalized by their corresponding first harmonic and amplified by the minimum first harmonic of the 4 cases. The smaller the indicator, the better the performance. The best performance occurs in the case that the inductance is on both sides for the cases tested, as expected from Fig. 6. Thus, the models for S_p and S_s, and the machine-learning model for the metrics describe the experimental results tested. Note that the magnitudes of the experimental results are higher than the theoretical ones, and the expected designs that achieve minimum harmonic content match the theoretical results. Besides, a recommended practice is to operate in a zone that is likely to achieve low harmonic content (flat zones), despite the fact that the minimum harmonic content might be in the middle of the inductance range. Moreover, dv/dt is a function of the voltage, the equivalent drain-source capacitance in the switches, and the current during switching, which are not simple to determine for all operating points. For the tests executed, t_r (the rising and falling time) is close to 200ns.

VI. DISCUSSION

In this section, the modeling of the ringing metric and its efficient evaluation through the ML model is shortly discussed and expanded to other potential optimization objectives.

A. ANN generalization

The value provided by the ML model lies in its potential for generalization, which is defined as the ability to perform well on previously unobserved inputs [31]. This involves preventing overfitting, which aims to capture data behavior without excessively increasing network weights size. *K-fold cross-validation* and *dropout* can also aid to achieve it [31]. Another recommended practice is the use of a regularization term in the loss function (e.g. L2 regularization of the weights), which helps to avoid a significant increment of the weight during each training epoch. Besides, shuffling the data set when drawing training batches helps in this aspect as well, and reduces the risk of the model learning patterns that are specific to the order of the data. By doing this, the resulting model is accurate within the bounds of the input variables in the training data set (or interpolating). In the case that the pattern is simple, and the model generalizes well within the bounds of its input data, the neural network might be able to make reasonable extrapolations. However, if complex patterns or data changes significantly outside the training range, the extrapolation can provide unreliable predictions. It is not recommended to use the model for every case as extrapolation, only interpolation.

B. Metrics for current ringing modeling and ANN

There is a large number of potential operating voltage conditions and magnetic tank impedance configurations that can be considered to operate and design the power converter, leading to many possible current ringing scenarios. From a voltage waveform point of view, higher switching frequency due to SiC and GaN switches will increase the bandwidth of interest. From an impedance point of view, a potentially more complex high-frequency model can be necessary, where other parameters or considerations can be relevant to include. In this sense, the present methodology can provide a generalized machine-learning model that can learn the features of the metrics, and thus allow a rapid evaluation of multiple scenarios and help the converter designer to study the performance of the high-frequency harmonic content.

C. Use of AI, ML and ANN for optimization problems

The challenge of designing complex systems with multiple conflicting objectives (or targets), such as minimizing cost, volume, weight, losses, and failure rate, can be framed as a multi-objective optimization problem. The current ringing can be added as another objective. In this context, each design parameter serves as an input variable that influences the output targets. The quest to find an optimal design that balances these objectives requires exploring a potential extensive design space, which can be highly time-consuming. This is particularly true for complex systems with intricate models that require significant computational resources and time for evaluation.

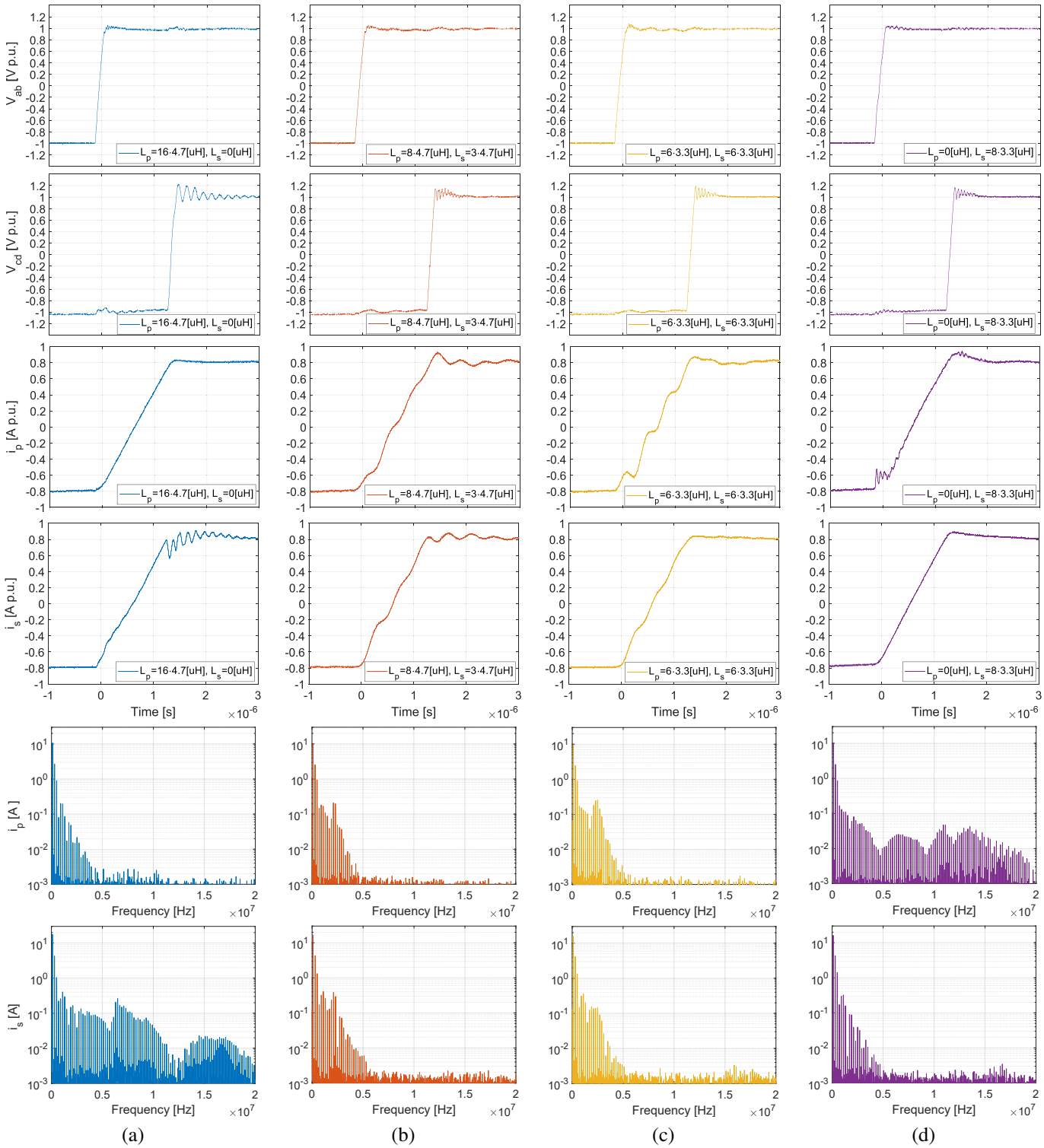

Fig. 9. Experimental results from oscilloscope data points for f_{sw} = 100kHz and D_3 = 0.275. v_{ab} normalized by v_{dc1} = 520V, v_{cd} normalized by v_{dc2} = 306V, and currents (normalized by its fundamental component for $i_p(t)$ and $i_s(t)$ in rows 3 and 4). First row: $v_{ab}(t)$; second row: $v_{cd}(t)$; third row: $i_p(t)$; forth row: $i_s(t)$; fifth row: $i_p(f)$; sixth row: $i_s(f)$. (a) $L_p = 16 \cdot 4.7\mu H$, $L_s = 0\mu H$; (b) $L_p = 8 \cdot 4.7\mu H$, $L_s = 3 \cdot 4.7\mu H$; (c) $L_p = 6 \cdot 3.3\mu H$, $L_s = 6 \cdot 3.3\mu H$; (d) $L_p = 0\mu H$, $L_s = 8 \cdot 3.3\mu H$.

Modern AI and ML approaches have emerged as effective tools to address the computational challenges associated with design optimization in power electronic systems. Article [32] analyzed 444 relevant journal papers up to May 2020. Considering the context explained in the last paragraph, two relevant tasks can be addressed for optimization problems using AI, regression models, and optimization/searching algorithms.

Regression ML models can be used to rapidly and precisely evaluate the influence of the design parameters over the objectives or other variables to help model them. To create

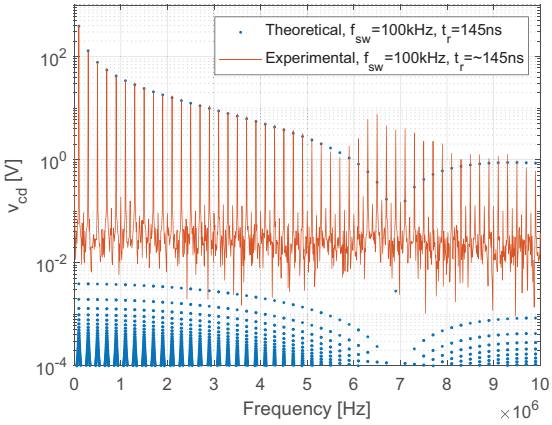

(a) Magnetic tank A: $L_p = 16 \cdot 4.7\mu H$, $L_s = 0\mu H$.

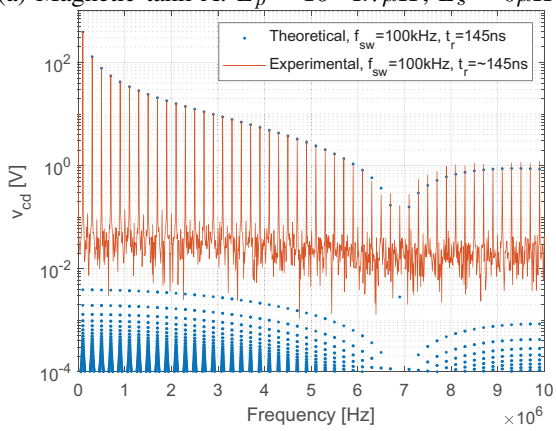

(b) Magnetic tank D: $L_p = 0\mu H$, $L_s = 8 \cdot 3.3\mu H$.

Fig. 10. Theoretical and experimental voltage spectrum of v_{cd} (considering $v_{dc2} = 306V$) for magnetic tank with inductances only in primary (a) and secondary (b) sides.

the model, one of the main tasks is the data set generation, which can be obtained via simulations (e.g. using numerical models like finite-element modeling, or dynamic simulation to get parameter performance in time), or analytical models (e.g. based on closed-form solutions of the parameters of interest), or a mix of them. Using these data an ML model can be trained and tested, which is done only one time. By having the ML model, it is possible to avoid multiple time-consuming simulations to assess more scenarios, which is very beneficial to the design process. ANN models can be trained for this purpose. They will consume less memory than storing the entire data set (to e.g. use a look-up table) since they store only the weights and biases of network units. Additionally, they are good at modeling nonlinearities without incurring significant memory overhead. For example, [33] demonstrated the use of ANN to rapidly estimate the effect of different design parameters over the yearly lifetime consumption (LC) of the semiconductors in a power converter PV system. Thanks to this, the Pareto front that describes the grid filter inductor and the LC can be rapidly modeled. Similarly, [34] used ANN to model the thermal and magnetic performance (see Table 3 of [34]) of an inductor for different magnetic design parameters (see Table 2 of [34]), which was used to model the Pareto front for multiple designs in a short period of time. While ANN offers substantial benefits, other ML methods can be explored as well. For instance, Gaussian Process Regression (GPR) offers advantages like uncertainty quantification, which can be used for making informed decisions in design optimization.

For optimization, different programs can be used to explore the design space and find the design parameters that minimize the objectives. In AI, the main options used are metaheuristic methods [32] (e.g. genetic algorithms, particle swarm). Using these algorithms, the exploration for the optimal solution uses randomness to evaluate via trial-and-error the influences of the design parameters over the targets. This type of search algorithm does not guarantee to find the global optimum but reduces the computational effort and time to get a solution. Besides, it balances exploration and exploitation, enabling for searching new areas and avoiding getting trapped in local optima. By incorporating a variety of ML methods, the optimization of complex designs can be further enhanced, allowing designers to evaluate an array of performance metrics, and enabling automated design processes that encompass multiple objectives and variables.

VII. Conclusions

The present article describes, theoretically and experimentally, the relationship between the voltage harmonic content and the impedance of the magnetic tank that will generate current ringing on the transformer's primary and secondary sides. A metric to measure this phenomenon is derived and discussed. It is based on the switching frequency, the rising and falling time of the voltage waveform on primary and secondary sides, the dc-link primary and secondary voltages, the magnetic tank inductances, and its stray capacitance values on each side. Then, a model of the metric for the primary and secondary sides (S_p and S_s) is trained and tested, considering the above-commented inputs. This results in a model that can represent the data set for different SRF values, primary and secondary side inductances, switching frequencies and dv/dt values, under the nominal input and output voltage. The model considers the parameters obtained via an impedance analyzer, which does not account for any shifting of the parameters due to thermal or aging processes. This will vary the harmonic content of the high-frequency currents during the lifespan of the converter. Experimental results are presented to contrast the models, which validates the quantitatively represented performance. We noted that tolerance is an important factor to consider, as it defines a zone where the current performance will behave within certain bounds. The criterion of how to select the inductance value is validated using the metric models. The methodology makes use of a steady-state frequency analysis via FFT.

Future work might consider a more complex model to design how the current ringing can be generated, and incorporate mitigation measures at the design stage. More aspects can be considered in the trained model, such as efficiency or other factors that can be correlated or may be relevant for analyze. Other metrics may be used to evaluate the harmonic performance, with the same methodology that has been developed.

The proposed methodology should be particularly interesting for high-frequency multi-active bridge converters [35]–

[38], where potentially many dv/dt sources can be considered. These fall outside the scope of the present study, but an analogously methodology is applicable.

VIII. Appendix

A. Metric for primary and secondary harmonic content

Considering that the core of the magnetic components will not be saturated, the magnetic tank can be modeled as a linear plant. Thus, source superposition can be applied. We define i_{pp} (and analogously for i_{ss}) as the primary side current generated by the primary side voltage v_{ab} short-circuiting the secondary (i.e. $v_{cd} = 0$). Thus, the primary and secondary currents i_p and i_s can be modeled in Eqn. (6), where n is the transformer's turn-ratio.

$$\begin{pmatrix} i_p \\ i_s \end{pmatrix} = \begin{pmatrix} 1 & -1/n \\ n & -1 \end{pmatrix} \cdot \begin{pmatrix} i_{pp} \\ i_{ss} \end{pmatrix} \tag{6}$$

Consider that $i_{pp} = v_{ab}/Z^p_{in}$ and $i_{ss} = v_{cd}/Z^s_{in}$. The currents i_{pp} and i_{ss} are modeled in the complex plane. To describe the high-frequency harmonic content without reducing significantly the low amplitude values by powering by two each harmonic, a metric for each current is proposed in Eqn. (5). Thus, $i_{pp} \to S_p$ and $i_{ss} \to S_s$. Subtracting the fundamental component of i_p and i_s in Eqn. (6), and considering the metric defined in Eqn. (5), it results in Eqn. (7).

$$\begin{aligned} i_p - i_p(f_{sw}) &= i_{pp}(f_{sw}) \cdot S_p - n^{-1} \cdot i_{ss}(f_{sw}) \cdot S_s \\ i_s - i_s(f_{sw}) &= n \cdot i_{pp}(f_{sw}) \cdot S_p - i_{ss}(f_{sw}) \cdot S_s \end{aligned} \tag{7}$$

The fundamental component of i_{pp} and i_{ss} are defined in Eqn. (8), where $v^x_{\sqcap}(f)$ represents the harmonic content of a unitary square ac signal of rising and falling time t_r (x=p for primary and x=s for secondary). It is considered that $Z^p_{in}(f_{sw}) \approx n^2 Z^s_{in}(f_{sw}) \approx 2\pi f_{sw} L$.

$$\begin{aligned} i_{pp}(f_{sw}) &= \frac{v_{dc1} \cdot v^p_{\sqcap}(f_{sw})}{2\pi f_{sw} L} \\ i_{ss}(f_{sw}) &= \frac{v_{dc2} \cdot v^s_{\sqcap}(f_{sw})}{2\pi f_{sw} L/(n^2)} \end{aligned} \tag{8}$$

For the DAB it is defined $d = \frac{n v_{dc2}}{v_{dc1}}$. Thus, assuming that $v^p_{\sqcap}(f_{sw}) \approx v^s_{\sqcap}(f_{sw})$, from Eqn. (8) we can define a relationship $i_{pp}(f_{sw})$ and $i_{ss}(f_{sw})$ in Eqn. (9).

$$i_{pp}(f_{sw}) = (nd)^{-1} i_{ss}(f_{sw}) \tag{9}$$

Thus, considering Eqn. (9), normalizing by $i_{pp}(f_{sw})$ and $i_{ss}(f_{sw})$ the Eqn. (7), results in Eqn. (10), which represents the normalized harmonic content for each side.

$$\frac{i_p - i_p(f_{sw})}{i_{pp}} = d \frac{i_s - i_s(f_{sw})}{i_{ss}} = S_p - dSs \tag{10}$$

We define the metric M^p that represents the normalized harmonic content of the transformer's primary side current. Analogously for the secondary, $M^s = M^p/d$. Finally, by selecting the value of $d \approx 1$ (by setting the input and output voltages accordingly), and considering that S_p and S_s are the sums of the amplitudes, where no phase is considered, the metric to evaluate the joint effect that primary and secondary produces is proposed in Eqn. (11).

$$M = M^p = M^s = S_p + S_s \tag{11}$$

References

[1] R. De Doncker, D. Divan, and M. Kheraluwala, "A three-phase soft-switched high-power-density dc/dc converter for high-power applications," *IEEE Transactions on Industry Applications*, vol. 27, no. 1, pp. 63–73, 1991.

[2] S. Shao, H. Chen, X. Wu, J. Zhang, and K. Sheng, "Circulating current and zvs-on of a dual active bridge dc-dc converter: A review," *IEEE Access*, vol. 7, pp. 50 561–50 572, 2019.

[3] S. Shao, L. Chen, Z. Shan, F. Gao, H. Chen, D. Sha, and T. Dragičević, "Modeling and advanced control of dual-active-bridge dc–dc converters: A review," *IEEE Transactions on Power Electronics*, vol. 37, no. 2, pp. 1524–1547, 2022.

[4] S. Shao, M. Jiang, W. Ye, Y. Li, J. Zhang, and K. Sheng, "Optimal phase-shift control to minimize reactive power for a dual active bridge dc-dc converter," *IEEE Transactions on Power Electronics*, vol. 34, no. 10, pp. 10 193–10 205, 2019.

[5] M. H. Rashid, *Power Electronics Handbook*, 3rd ed. Elsevier Inc., 2011.

[6] H. W. Otto, *Electromagnetic Compatibility Engineering*. John Wiley and Sons, 2009.

[7] B. K. Bose, *Power Electronics and Motor Drives - Advances and Trends*. Elsevier Inc., 2021.

[8] X. Wang, M. Sandell, G. Watkins, K. Shusuke, U. Takeshi, and O. Kohei, "Ringing loss analysis and its influence on boost converter efficiency," in *11th International Conference on Power Electronics, Machines and Drives (PEMD 2022)*, vol. 2022, 2022, pp. 97–101.

[9] B. Cui, H. Shi, Q. Sun, X. Tang, L. Hong, and B. Zhao, "A novel analysis, design, and optimal methodology of high-frequency oscillation for dual active bridge converters with wbg switching devices and nanocrystalline transformer cores," *IEEE Transactions on Power Electronics*, vol. 36, no. 7, pp. 7665–7678, 2021.

[10] N. Oswald, P. Anthony, N. McNeill, and B. H. Stark, "An experimental investigation of the tradeoff between switching losses and emi generation with hard-switched all-si, si-sic, and all-sic device combinations," *IEEE Transactions on Power Electronics*, vol. 29, no. 5, pp. 2393–2407, 2014.

[11] Z. Fang, D. Jiang, and Y. Zhang, "Study of the characteristics and suppression of emi of inverter with sic and si devices," *Chinese Journal of Electrical Engineering*, vol. 4, no. 3, pp. 37–46, 2018.

[12] *Switch Node Ring Control in Synchronous Buck Regulators*, ON Semiconductor, 2013. [Online]. Available: https://www.onsemi.com/pub/collateral/an-4162.pdf

[13] R. Severns, *Design of snubbers for power circuits.* [Online]. Available: https://www.cde.com/resources/technical-papers/design.pdf

[14] M. Kheraluwala, R. Gascoigne, D. Divan, and E. Baumann, "Performance characterization of a high-power dual active bridge dc-to-dc converter," *IEEE Transactions on Industry Applications*, vol. 28, no. 6, pp. 1294–1301, 1992.

[15] J. Zhang, J.-S. Lai, R.-Y. Kim, and W. Yu, "High-power density design of a soft-switching high-power bidirectional dc–dc converter," *IEEE Transactions on Power Electronics*, vol. 22, no. 4, pp. 1145–1153, 2007.

[16] W. Xu, A. Vetrivelan, Z. Guo, R. Yu, and A. Q. Huang, "Efficiency optimization of dual active bridge converter based on dv/dt snubber capacitors," in *2021 IEEE Applied Power Electronics Conference and Exposition (APEC)*, 2021, pp. 647–653.

[17] Y. Ting, S. de Haan, and J. A. Ferreira, "Efficiency improvements in a single active bridge modular dc-dc converter with snubber capacitance optimisation," in *2014 International Power Electronics Conference (IPEC-Hiroshima 2014 - ECCE ASIA)*, 2014, pp. 2787–2793.

[18] Y. Ting, S. de Haan, and B. Ferreira, "Modular single-active bridge dc-dc converters: Efficiency optimization over a wide load range," *IEEE Industry Applications Magazine*, vol. 22, no. 5, pp. 43–52, 2016.

[19] H. Huang, X. Yang, Y. Wen, and Z. Long, "A switching ringing suppression scheme of sic mosfet by active gate drive," in *2016 IEEE 8th International Power Electronics and Motion Control Conference (IPEMC-ECCE Asia)*, 2016, pp. 285–291.

[20] J. J. O. Dalton, H. C. P. Dymond, J. Wang, M. H. Hedayati, D. Liu, D. Drury, and B. H. Stark, "Stretching in time of gan active gate driving profiles to adapt to changing load current," in *2018 IEEE Energy Conversion Congress and Exposition (ECCE)*, 2018, pp. 3497–3502.

[21] C. Krause, A. Bendicks, and S. Frei, "Active gate control with synthesized signals to avoid overshoots and ringing in dc-to-dc converters," in *PCIM Europe digital days 2021; International Exhibition and Conference for Power Electronics, Intelligent Motion, Renewable Energy and Energy Management*, 2021, pp. 1–7.

[22] A. P. Camacho, V. Sala, H. Ghorbani, and J. L. R. Martinez, "A novel active gate driver for improving sic mosfet switching trajectory," *IEEE Transactions on Industrial Electronics*, vol. 64, no. 11, pp. 9032–9042, 2017.
[23] H. Zhao, S. Luan, Z. Shen, A. J. Hanson, Y. Gao, D. N. Dalal, R. Wang, S. Zhou, and S. Munk-Nielsen, "Rethinking basic assumptions for modeling parasitic capacitance in inductors," *IEEE Transactions on Power Electronics*, vol. 37, no. 7, pp. 8281–8289, 2022.
[24] M. Pahlevaninezhad, D. Hamza, and P. K. Jain, "An improved layout strategy for common-mode emi suppression applicable to high-frequency planar transformers in high-power dc/dc converters used for electric vehicles," *IEEE Transactions on Power Electronics*, vol. 29, no. 3, pp. 1211–1228, 2014.
[25] Y. Li, H. Zhang, S. Wang, H. Sheng, C. P. Chng, and S. Lakshmikanthan, "Investigating switching transformers for common mode emi reduction to remove common mode emi filters and y-capacitors in flyback converters," *IEEE Journal of Emerging and Selected Topics in Power Electronics*, vol. 6, no. 4, pp. 2287–2301, 2018.
[26] Z. Ouyang, O. C. Thomsen, and M. A. E. Andersen, "Optimal design and tradeoff analysis of planar transformer in high-power dc–dc converters," *IEEE Transactions on Industrial Electronics*, vol. 59, no. 7, pp. 2800–2810, 2012.
[27] Z. Qin, Z. Shen, F. Blaabjerg, and P. Bauer, "Transformer current ringing in dual active bridge converters," *IEEE Transactions on Industrial Electronics*, vol. 68, no. 12, pp. 12 130–12 140, 2021.
[28] M. L. Heldwein, "Emc filtering of three/phase pwm converters," PhD dissertation, ETH Zurich, 2008.
[29] J. Everts, "Closed-form solution for efficient zvs modulation of dab converters," *IEEE Transactions on Power Electronics*, vol. 32, no. 10, pp. 7561–7576, 2017.
[30] C. Østergaard, C. S. Kjeldsen, and M. Nymand, "Calculation of planar transformer capacitance based on the applied terminal voltages," in *2020 IEEE 21st Workshop on Control and Modeling for Power Electronics (COMPEL)*, 2020, pp. 1–7.
[31] I. Goodfellow, Y. Bengio, and A. Courville, *Deep Learning*. MIT Press, 2016, http://www.deeplearningbook.org.
[32] S. Zhao, F. Blaabjerg, and H. Wang, "An overview of artificial intelligence applications for power electronics," *IEEE Transactions on Power Electronics*, vol. 36, no. 4, pp. 4633–4658, 2021.
[33] T. Dragičević, P. Wheeler, and F. Blaabjerg, "Artificial intelligence aided automated design for reliability of power electronic systems," *IEEE Transactions on Power Electronics*, vol. 34, no. 8, pp. 7161–7171, 2019.
[34] T. Guillod, P. Papamanolis, and J. W. Kolar, "Artificial neural network (ann) based fast and accurate inductor modeling and design," *IEEE Open Journal of Power Electronics*, vol. 1, pp. 284–299, 2020.
[35] M. Neubert, "Modeling, synthesis and operation of multiport-active bridge converters," PhD dissertation, RWTH Aachen University, 2020.
[36] Y.-K. Tran, "Multiport energy gateway," PhD dissertation, École Polytechnique Fédérale de Lausanne, 2019.
[37] S. Bandyopadhyay, P. Purgat, Z. Qin, and P. Bauer, "A multiactive bridge converter with inherently decoupled power flows," *IEEE Transactions on Power Electronics*, vol. 36, no. 2, pp. 2231–2245, 2021.
[38] M. Liu, Y. Chen, Y. Elasser, and M. Chen, "Dual frequency hierarchical modular multilayer battery balancer architecture," *IEEE Transactions on Power Electronics*, vol. 36, no. 3, pp. 3099–3110, 2021.

Miguel E. López Gajardo earned the Ingeniero Civil Electrónico degree and M.Sc. in Electronic Engineering from the Universidad Técnica Federico Santa María, Valparaíso, Chile, in 2014. He worked in the Advanced Center for Electrical and Electronic Engineering (AC3E) as R&D Engineer from 2015 to 2020. He is pursuing a Ph.D. degree at the Technical University of Denmark (DTU), as part of the Department of Wind and Energy Systems. His research interests include power electronics, e-mobility, renewable energy conversion systems, drives, AI, and their applications.

Pere Izquierdo Gómez (S'22) received the B.Sc. degree in energy engineering from the Polytechnic University of Catalonia, Barcelona, Spain, in 2018, and the M.Sc. degree in energy engineering from Aalborg University, Aalborg, Denmark, in 2020. He is currently pursuing the Ph.D. degree in the Technical University of Denmark (DTU), as part of the Department of Wind and Energy Systems, working on power converter diagnostics and control with a focus on machine learning applications.

Nenad Mijatovic (nemi@dtu.dk) after obtaining his Dipl.Ing. education in Electrical Power Engineering at University of Belgrade, Serbia in 2007, was enrolled as a doctoral candidate at Technical University of Denmark. He received his Ph.D. degree from Technical University of Denmark for his work on technical feasibility of novel machines and drives for wind industry. Upon completion of his PhD, he continued work within the field of wind turbine direct-drive concepts as an Industrial PostDoc. Dr. N. Mijatovic currently holds position of Associate Professor at Technical University of Denmark where he is in charge of managing research projects and education related to the field of electrical machines and drives, power electronic convertors, motion control, application of energy storage and general applications of low frequency electromagnetism and large scale application of superconductivity with main focus on emerging eMobility and renewable energy generation. He is a member of IEEE since 2008 and senior member of IEEE since 2018 and his field of interest and research includes novel electrical machine drives/actuator designs, operation, control and diagnostic of electromagnetic assemblies, advance control of drives and grid connected power electronics, energy storage and eMobility.

José Rodríguez (jose.rodriguezp@uss.cl) (M'81-SM'94-F'10-LF'20) received the Engineer degree in electrical engineering from the Universidad Tecnica Federico Santa Maria, in Valparaiso, Chile, in 1977 and the Dr.-Ing. degree in electrical engineering from the University of Erlangen, Erlangen, Germany, in 1985. He has been with the Department of Electronics Engineering, Universidad Tecnica Federico Santa Maria, since 1977, where he was full Professor and President. Since 2015 to 2019 he was the President of Universidad Andres Bello in Santiago, Chile. Since 2022 he is President of Universidad San Sebastian in Santiago, Chile. He has coauthored two books, several book chapters and more than 700 journal and conference papers. His main research interests include multilevel inverters, new converter topologies, control of power converters, and adjustable-speed drives. He has received a number of best paper awards from journals of the IEEE. Dr. Rodriguez is member of the Chilean Academy of Engineering. In 2014 he received the National Award of Applied Sciences and Technology from the government of Chile. In 2015 he received the Eugene Mittelmann Award from the Industrial Electronics Society of the IEEE. In years 2014 to 2022 he has been included in the list of Highly Cited Researchers published by Web of Science.

Tomislav Dragičević (tomdr@dtu.dk) earned his M.Sc. and industrial Ph.D. degrees in electrical engineering from the Faculty of Electrical Engineering, Zagreb, Croatia, in 2009 and 2013, respectively. He is currently a professor at Technical University of Denmark, where he leads research in the digitization of power converters. He has published more than 150 IEEE journal articles in these areas. He serves as associate editor of IEEE Transactions on Industrial Electronics and IEEE Emerging and Selected Topics in Power Electronics and an editor of IEEE Industrial Electronics Magazine. He is a Senior Member of the IEEE.